

1 **P wave anisotropy caused by partial eclogitization of descending crust demonstrated**  
2 **by modelling effective petrophysical properties**

3 This is a non peer-reviewed preprint from earthArxiv, submitted to *Geochemistry, Geophysics,*  
4 *Geosystems*

5  
6 **Sascha Zertani<sup>1\*</sup>, Johannes C. Vrijmoed<sup>1</sup>, Frederik Tilmann<sup>1,2</sup>, Timm John<sup>1\*</sup>, Torgeir B.**  
7 **Andersen<sup>3</sup>, & Loic Labrousse<sup>4</sup>**

8 <sup>1</sup>Institute of Geological Sciences, Freie Universität Berlin, 12249, Berlin, Germany.

9 <sup>2</sup>Deutsches GeoForschungsZentrum, 14473, Potsdam, Germany.

10 <sup>3</sup>The Centre of Earth Evolution and Dynamics (CEED), Department of Geosciences, University  
11 of Oslo, 0316 Oslo, Norway.

12 <sup>4</sup>Sorbonne Université, CNRS-INSU, Institut des Sciences de la Terre Paris, IStEP, UMR 7193,  
13 F-75005 Paris, France.

14  
15 Corresponding authors:

16 Sascha Zertani, Department of Geosciences, Freie Universität Berlin, Malteserstr. 74-100,  
17 12249, Berlin, Germany. E-mail address: sascha.zertani@fu-berlin.de. Telephone: +49 30 838  
18 75782.

19 and

20 Timm John, Department of Geosciences, Freie Universität Berlin, Malteserstr. 74-100, 12249,  
21 Berlin, Germany. E-mail address: timm.john@fu-berlin.de. Telephone: +49 30 838 70103.

22 **Key Points:**

- 23 • Eclogitization of crustal rocks causes significant anisotropy on a crustal scale  
24 • Geometric arrangement has no significant influence on effective seismic properties  
25 • Backazimuthal bias in receiver function studies can be caused by eclogitization

**27 Abstract**

28 Seismological studies of large-scale processes at active convergent plate boundaries typically  
29 probe lower crustal structures with wavelengths of several kilometers, whereas field-based  
30 studies typically sample the resulting structures at a much smaller scale. To bridge this gap  
31 between scales we derive effective petrophysical properties on the 20-m, 100-m, and kilometer  
32 scales based on numerical modelling with the Finite Element Method. Geometries representative  
33 of eclogitization of crustal material are extracted from the partially eclogitized exposures on the  
34 island of Holsnøy (Norway). We find that the P wave velocity is controlled by the properties of  
35 the constituent lithologies rather than their geometric arrangement. P wave anisotropy, however,  
36 is dependent on the fabric orientation of the associated rocks, as fabric variations cause changes  
37 in the orientation of the initial anisotropy. As a result, different structural associations can result  
38 in effective anisotropies ranging from ~0-4% for eclogites not associated with ductile  
39 deformation to up to 8% for those formed during ductile deformation. For the kilometer-scale  
40 structures, a scale that in principle can be resolved by seismological studies, we obtained P wave  
41 velocities between 7.7 and 8.1 km s<sup>-1</sup>. The effective P wave anisotropy on the kilometer-scale is  
42 ~5% and thus explains the backazimuthal dependence of seismological images of, for example,  
43 the Indian lower crust currently underthrusting beneath the Himalaya. These results imply that  
44 seismic anisotropy could be the key to visualize structures in active subduction and collision  
45 zones that are currently invisible to geophysical methods and thus unravel the underlying  
46 processes active at depth.

47

**48 1. Introduction**

49 Convergent plate boundaries are among the most important sites of crustal reorganization and  
50 element recycling. There, crustal material is buried to great depths, recycled into the mantle,  
51 integrated into orogenic roots and in some cases also exhumed back to the surface. All of these  
52 processes result in the modification of crustal rocks through metamorphism and brittle and/or  
53 ductile deformation. However, these processes occur at depths inaccessible to direct observation.  
54 Thus, the structures that develop at depth are either studied by geophysical imaging methods or  
55 by investigating exhumed rocks that have been metamorphosed and/or deformed in the past (e.g.,  
56 Austrheim, 1987; Rondenay et al., 2008). Field-based studies of deep processes are restricted to  
57 rare exposures where mineral assemblages and structures are not substantially overprinted during  
58 exhumation (e.g., Austrheim, 1987; John & Schenk, 2003). In order to properly interpret seismic  
59 velocities in terms of metamorphic processes associated with large-scale tectonics such as

60 continental collision and subduction of oceanic plates we require knowledge of how seismic  
61 properties change with depth and lithology (e.g., Kind et al., 2012; Rondenay et al., 2008).  
62 However, while field-based studies include information down to the micron scale, geophysical  
63 imaging techniques employ wavelengths that are only sensitive to kilometer-scale structures  
64 (e.g., Bloch et al., 2018; Kim et al., 2019). In addition, the resolution of geophysical imaging is  
65 often further limited by the available station coverage and distribution of signal sources. This  
66 creates a large gap between the scale at which we image structures with geophysical methods  
67 and the scale at which we can observe structures in the field. Subsequently, seismic velocities  
68 that are measured in the laboratory or calculated for individual samples may not be  
69 representative of the properties of lithological and structural associations on a larger scale. As  
70 these structures are smaller than the resolution of seismological methods the properties of the  
71 different constituents will act together averaging to one effective medium (e.g., Backus, 1962;  
72 Hudson, 1981).

73 Specifically, eclogitization processes occurring at depth remain difficult to assess, although they  
74 are suspected to play a major role in geodynamic processes (Austrheim, 1991; Dewey et al.,  
75 1993; Yamato et al., 2019). Eclogitization causes a density increase of crustal material that  
76 decreases buoyancy forces and significantly adds to driving forces (e.g., slab pull) at convergent  
77 plate boundaries (e.g., Hetényi et al., 2007; Klemm et al., 2011). However, the same density  
78 increase also significantly complicates the detection of eclogites at depth as it is combined with  
79 an increase of the elastic moduli of the rock. Subsequently, the resulting seismic properties of  
80 eclogites become similar to those of mantle peridotites, making a distinction between the mantle  
81 and crust at depth difficult (e.g., Bostock, 2013; Hetényi et al., 2007; Rondenay et al., 2008;  
82 Yuan et al., 2000). Nevertheless, partially eclogitized material shows a range of geometric

83 configurations and patterns of anisotropy directions in the constituent lithologies, depending on  
84 conditions during formation (Raimbourg et al., 2005; Zertani et al., 2019b). It is therefore not  
85 necessarily straightforward to simply transform a measured velocity into a degree of  
86 eclogitization.

87 Field-based studies have shown that eclogitization of crustal rocks is often associated with fluid  
88 availability that enhances mineral reactions and ductile deformation, first forming centimeter-  
89 thick shear zones (Austrheim, 1987; John & Schenk, 2003). As eclogitization and deformation  
90 progress, such shear zones can widen reaching a thickness of a few hundred meters (Boundy et  
91 al., 1997; Raimbourg et al., 2005; Zertani et al., 2019b). In the exposed examples such structures  
92 rarely reach scales that can be resolved with geophysical methods and the complex associations  
93 would thus act as an effective medium at depth adapting averaged properties of the different  
94 lithologies (Zertani et al., 2019a).

95 In contrast, geophysical imaging methods are used to study large-scale processes active at great  
96 depth in collision and subduction zones (e.g., Halpaap et al., 2018). To unravel structures caused  
97 by metamorphism coeval with deformation, the receiver function method is of specific interest. It  
98 is based on the conversion of P to S waves and vice versa at boundaries with contrasting  
99 impedance and therefore mostly sensitive to structural boundaries (Kind et al., 2012). For  
100 example, Schneider et al. (2013) imaged a low velocity zone below the Pamir corresponding to  
101 the subducting lower continental crust of the Eurasian Plate. The velocity contrast of this zone  
102 with respect to the surrounding mantle, however, decreases below a depth of ~100 km,  
103 suggesting eclogitization of the down going crust. Nabelek et al. (2009) and Schulte-Pelkum et  
104 al. (2005) observed a backazimuthal dependence of the retrieved signal in the lower crust of

105 India beneath the Himalaya that suggests a significant large-scale anisotropic fabric within the  
106 lower continental crust of India.

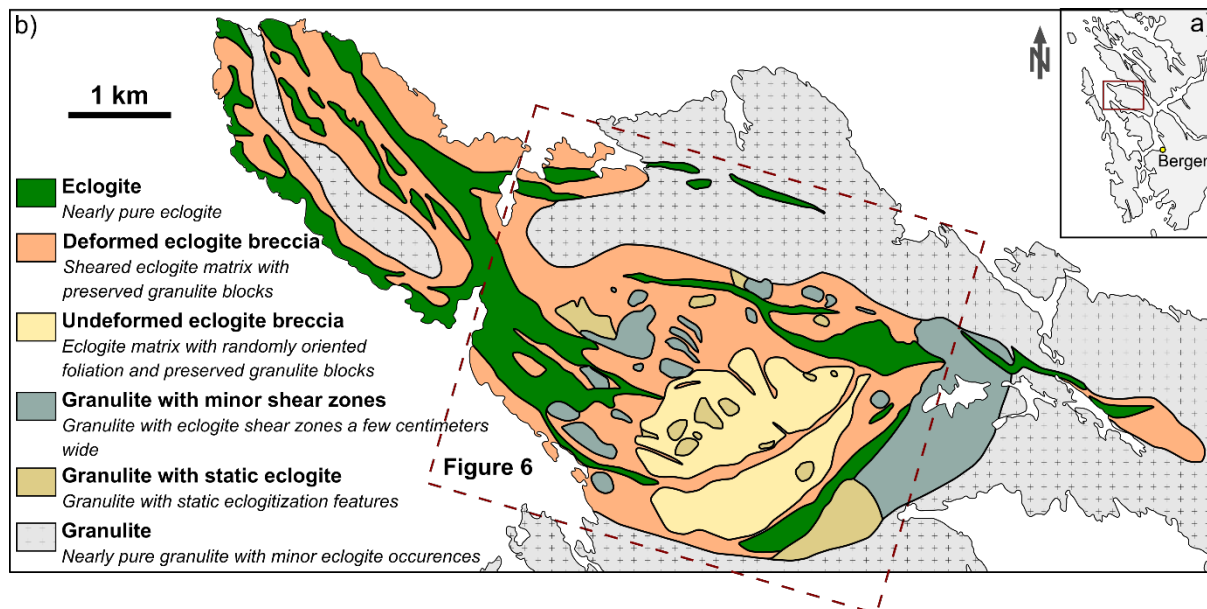
107 Meanwhile, direct estimates of seismic velocities are usually derived from samples that are only  
108 a few centimeters in size (e.g., Kern et al., 1996) and extrapolation to scales that are resolvable  
109 using geophysical methods relies on poorly supported assumptions, mainly that the composition  
110 of the samples is representative of the crust at geophysically relevant scale and that the large-  
111 scale organization of lithologies has no relevance. Voigt-Reuss-Hill averaging is the standard  
112 method to calculate velocities within a medium based on the abundance of individual mineral  
113 phases resulting in an average (isotropic) seismic velocity (Hill, 1952). The classic Backus  
114 averaging allow calculation of the effective anisotropy of a finely layered medium; it is valid  
115 under the assumption that the thickness of individual layers is far smaller than the seismic  
116 wavelength (Backus, 1962). Although such averaging schemes are widely used to constrain  
117 seismic velocities of various rocks, their capabilities are limited because they are only valid for  
118 simple geometries that generally do not capture the structural complexity of real rocks.

119 To assess these simplifying assumptions, it is necessary to utilize a more sophisticated approach.  
120 Accordingly, we calculate effective P wave velocities of eclogite-facies associations using a  
121 technique based on finite element method (FEM) calculations, for a variety of representative  
122 geometries. The simplified geometries are derived from the field observations on the island of  
123 Holsnøy in the Bergen Arcs (Norway), where a >70 km<sup>2</sup> large complex of partially eclogitized  
124 lower continental crust is exposed that provides an excellent coherent laboratory to study the  
125 geometries that are established during eclogitization.

## 126 **2. Geological Setting**

127 The exposed lower continental crust on the island of Holsnøy (Bergen Arcs, western Norway)

128 has been partially eclogitized during the Caledonian orogeny (Austrheim, 1991). The rocks  
 129 belong to the Lindås nappe, which together with the Dalsfjord and Jotun nappe complexes  
 130 represents the lower crust of the former Jotun microcontinent, that constituted part of the pre-  
 131 Caledonian hyperextended margin of Baltica (Andersen et al., 2012; Jakob et al., 2019). The  
 132 Lindås nappe is for a large part composed of anorthositic granulites that experienced Proterozoic  
 133 granulite-facies P-T conditions of  $\sim 1$  GPa and  $\sim 800$  °C, at  $\sim 950$  Ma (Austrheim & Griffin,  
 134 1985). The P-T conditions in the following  $\sim 500$  M.y. are unclear. The rocks, however, show no  
 135 signs of significant alteration before the Scandian Caledonian collision and likely cooled to  
 136 conditions reflecting mid to lower crustal conditions (Jamtveit et al., 1990).



137

138 **Fig. 1. Geological map of northwestern Holsnøy (modified from Jolivet et al. (2005) and Zertani et**  
 139 **al. (2019b)). The inset (a) shows the location of Holsnøy in western Norway.**

140

141 During the Caledonian collision the Jotun microcontinent constituted the leading edge of Baltica,  
 142 which was integrated into the collision wedge as the lower plate (Corfu et al., 2014).

143

144 Subsequently, the Lindås nappe was subjected to peak eclogite-facies conditions of  $\sim 2$  GPa and  
 $\sim 750$  °C at 429 Ma (Bhowany et al., 2018; Glodny et al., 2008; Jamtveit et al., 1990; Zhong et

145 al., 2019). Large volumes of the dry granulite-facies rocks, however, remained metastable and  
146 were thus preserved (Austrheim, 1987; Jackson et al., 2004). Eclogitization is linked to fluid  
147 availability and was facilitated along shear zones but also progressed into the rock volume as a  
148 static overprint (Austrheim, 1987; Zertani et al., 2019b). Fluid infiltration was likely initiated via  
149 brittle fractures, which provided fluid pathways within an otherwise dry rock (Austrheim, 1990;  
150 Jamtveit et al., 1990).

151 This heterogeneously distributed transformation resulted in a complex mixture of eclogites and  
152 granulites (Fig. 1). The resulting lithologies can be divided into six categories based on the  
153 abundance of eclogite and the associated structural relationships (Boundy et al., 1992; Zertani et  
154 al., 2019b). Next to the mostly unaltered granulite (<20 % eclogite), small-scale eclogitization  
155 features are distinguished into granulites cut by eclogite-facies shear zones a few centimeters  
156 wide and granulites with eclogitized patches that are not associated with ductile deformation  
157 (both 20-50 % eclogite). With progressive eclogitization these evolve into the so-called eclogite  
158 breccia, which can be described by two endmembers: sheared eclogite breccia composed of a  
159 strongly sheared eclogite matrix containing preserved granulite blocks and unsheared eclogite  
160 breccia, where the eclogite matrix was not subjected to pervasive ductile deformation (50-90 %  
161 eclogite). Ultimately, shear zones evolve that are up to a few hundred meters thick and are  
162 almost entirely composed of eclogite with little to no preserved granulite (>90 % eclogite).

### 163 **3. Model Setup**

164 The aim of this study is to obtain effective P wave velocities and the corresponding P wave  
165 anisotropy from variably eclogitized lower crustal rocks based on observed 2D geometric  
166 arrangements that act as an effective medium. Both the effective medium and the individual rock

167 types are treated as linear elastic anisotropic material for which Hooke's law gives the  
 168 relationship between stress ( $\sigma_{ij}$ ) and strain ( $\varepsilon_{kl}$ ):

$$169 \quad \sigma_{ij} = c_{ijkl} \varepsilon_{kl}$$

170 In 2D the 2x2x2x2 elastic tensor, which we represent by a symmetric 3-by-3 matrix in Voigt  
 171 notation (using the mapping 11→1, 22→2 and 12→3), is sufficient to fully describe the in-plane  
 172 anisotropy:

$$173 \quad \begin{bmatrix} c_{11} & c_{12} & c_{13} \\ c_{21} & c_{22} & c_{23} \\ c_{31} & c_{32} & c_{33} \end{bmatrix}$$

174 Due to symmetry considerations  $c_{13}$ ,  $c_{23}$ ,  $c_{31}$ , and  $c_{32}$  are expected to be zero, and  $c_{12}$  should be  
 175 equal to  $c_{21}$ . One way of obtaining the effective properties is to run numerical experiments  
 176 solving the elasto-dynamic wave equations and recording the time necessary for a wave to travel  
 177 through the medium (e.g., Saenger et al., 2004). Alternatively, we calculate the P wave velocities  
 178 from the elastic tensor of the effective medium using the formulas for transversely isotropic  
 179 media (Mavko et al., 2009):

$$180 \quad V_P = (c_{11} \sin^2 \theta + c_{22} \cos^2 \theta + c_{33} + \sqrt{M})^{\frac{1}{2}} (2\rho)^{-1/2}$$

181 where:

$$182 \quad M = [(c_{11} - c_{33}) \sin^2 \theta - (c_{22} - c_{33}) \cos^2 \theta]^2 + (c_{12} - c_{33})^2 \sin^2 2\theta$$

183 The individual components of the 2D elastic tensor ( $c_{ijkl}$ ) of the effective medium are calculated  
 184 from the stresses and strains calculated in a set of numerical experiments. For this purpose, three  
 185 experiments (Fig. 3) are performed for each geometric model, applying different boundary  
 186 conditions: (1) The area of interest is compressed along the y axis along the upper and lower  
 187 boundary by imposing a fixed displacement. Along the left and right boundary displacement in x  
 188 direction is zero. (2) The medium is compressed horizontally, that is, along the x axis. In this



189 case displacement in y direction is zero along the top and bottom boundary. (3) Finally, simple  
 190 shear is enforced along the top and bottom boundary, that is, displacement to the right along the  
 191 top boundary and to the left at the bottom boundary, resulting in shear parallel to the x axis. A  
 192 fourth experiment (simple shear parallel to the y axis) was used for validation and yielded the  
 193 same results as experiment (3), as is required from the symmetry of the elasticity tensor.  
 194 The three experiments result in a set of nine equations for six unknown components of the stress  
 195 tensor, so only 6 of these equations are needed. Due to the setup of each experiment specific  
 196 strains are zero which allows to simplify the equations to:

$$197 \quad c_{21} = \frac{\sigma_{xx}}{\varepsilon_{yy}}, c_{22} = \frac{\sigma_{yy}}{\varepsilon_{yy}}, \text{ and } c_{23} = \frac{\sigma_{xy}}{\varepsilon_{yy}}$$

198 for experiment 1,

$$199 \quad c_{11} = \frac{\sigma_{xx}}{\varepsilon_{xx}}, c_{12} = \frac{\sigma_{yy}}{\varepsilon_{xx}}, \text{ and } c_{13} = \frac{\sigma_{xy}}{\varepsilon_{xx}}$$

200 for experiment 2, and

$$201 \quad c_{31} = \frac{\sigma_{xx}}{\varepsilon_{xy}}, c_{32} = \frac{\sigma_{yy}}{\varepsilon_{xy}}, \text{ and } c_{33} = \frac{\sigma_{xy}}{\varepsilon_{xy}}$$

202 for experiment 3.

203 To extract the elastic properties of the effective medium, strain ( $\varepsilon_{kl}$ ) and stress ( $\sigma_{ij}$ ) are averaged  
 204 along the appropriate boundary. During vertical compression (experiment 1) strain and stress are  
 205 averaged along the top and bottom boundary giving the components of the elastic tensor that  
 206 describe the properties of the effective medium in y direction ( $c_{21}$ ,  $c_{22}$ , and  $c_{23}$ ). Equivalently,  
 207 strain and stress are averaged at the left and right boundary during horizontal compression  
 208 (experiment 2), giving the components of the elastic tensor describing the x direction ( $c_{11}$ ,  $c_{12}$ ,  
 209 and  $c_{23}$ ). Finally, during the simple shear experiment strain and stress at the top and bottom  
 210 boundary are averaged giving the remaining components of the elastic tensor ( $c_{31}$ ,  $c_{32}$ , and  $c_{33}$ ).  
 211 The boundaries at which the displacement for each of the experiments is enforced are kept far

212 away from the medium of interest to avoid boundary effects. Strain and stress are then averaged  
213 along the inner boundary surrounding only the medium of interest (red in Fig. 3). In those  
214 examples modelling the P wave velocities of the small-scale shear zones and the small-scale  
215 static overprint the eclogite is in contact with the inner boundary in some cases. Here the eclogite  
216 was extended into the area between inner and outer boundary to avoid edge effects.

217 The P wave velocities of the effective medium can then be calculated from the resulting 2D  
218 elastic tensor. Bulk density is obtained by calculating the mean of the densities weighted by the  
219 area of the granulite and eclogite used for the calculation. Note that the 2D elastic tensor is not  
220 sufficient to adequately describe S wave velocities because it does not describe the material  
221 properties for an S wave polarized perpendicular to the plane.

222 The calculations are performed, using the finite element method (FEM), employing an irregular  
223 triangular grid. Meshing is done using the mesh generator triangle (Shewchuk, 1996). Each  
224 triangular element consists of six nodes in which the displacement field is calculated and  
225 interpolation between the nodes is quadratic.

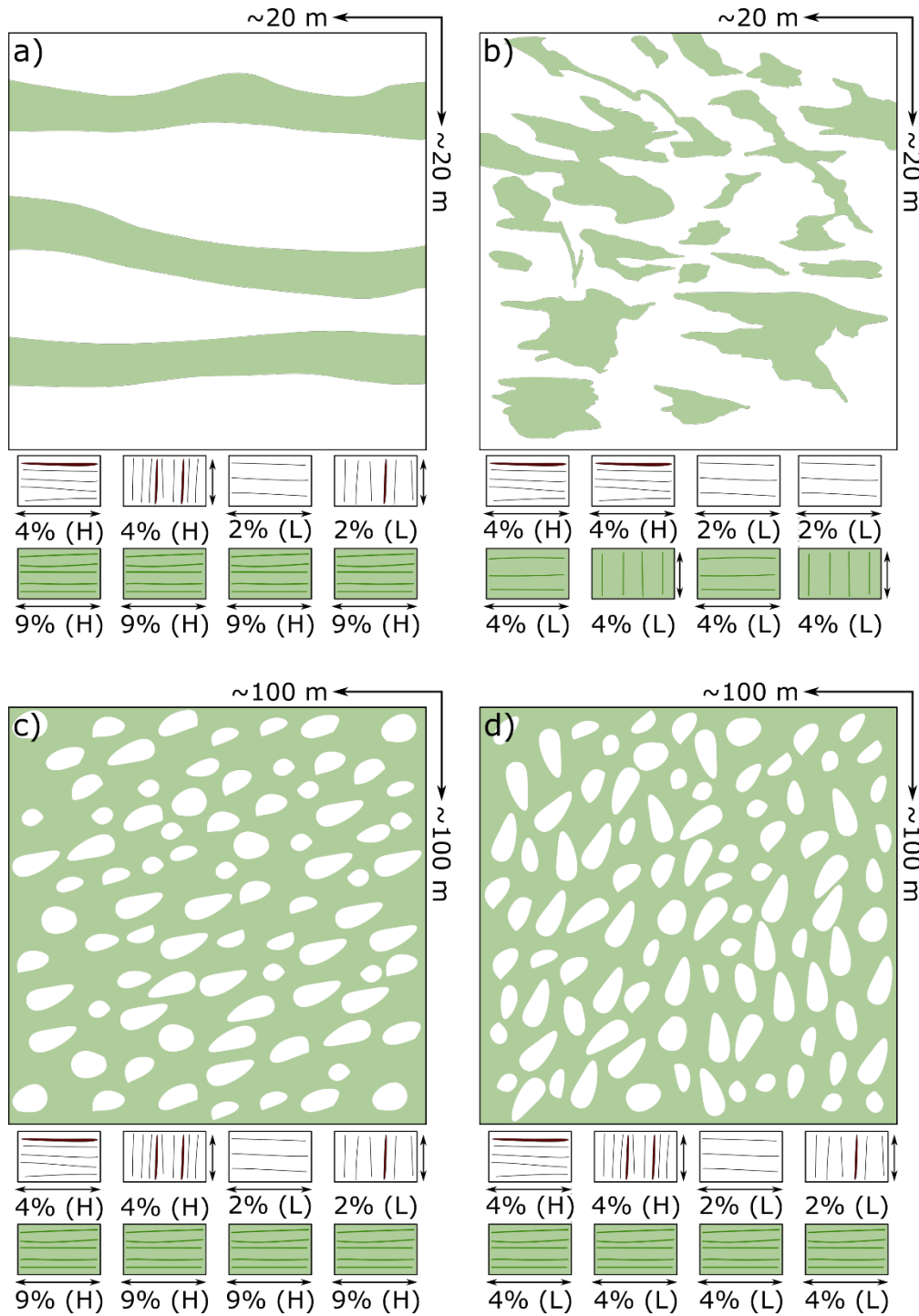
226 The method of obtaining the P wave velocity described above was tested and benchmarked using  
227 a layered medium, a problem for which an analytical solution exists (Backus, 1962), and  
228 resulting P wave velocities were, within 0.5% error, those calculated from the analytical solution.

229 The physical properties for each element representing the different material are given by the  
230 elastic tensor of the corresponding lithology, i.e., granulite or eclogite. Representative elastic  
231 tensors were calculated from the velocity measurements (x-z plane) in Zertani et al. (2019a).  
232 From this data, each component can be calculated separately with the exception of  $C_{12}$ , as this  
233 would require information on the variation of elastic wave speeds along oblique directions not  
234 available from laboratory measurements. Therefore, we simply used the mean P wave velocity

235 between the x and z axis to approximate the velocity of a P wave travelling at a 45° angle to the  
 236 foliation. In order to test the relative influence of the intrinsic properties of the constituting  
 237 lithologies and the geometries themselves, we used two different eclogites and two different  
 238 granulites (Tab. 1). Because the eclogites measured by Zertani et al. (2019a) were all collected  
 239 from the main shear zones exposed on Holsnøy, they all have a high P wave anisotropy. In order  
 240 to estimate effective properties for statically eclogitized areas, where the eclogite would likely  
 241 have a lower initial anisotropy, we assumed a lower velocity in x direction for one of the samples  
 242 (N-101 in Zertani et al., 2019a), thus giving a lower P wave anisotropy of 4%, which is in  
 243 accordance with others reported from Holsnøy (Fountain et al., 1994). Specifically, we chose to  
 244 use the velocity measured at lower confining pressure (600 MPa). This way, while the velocity is  
 245 artificially reduced it is still a function of the existing mineral assemblage.

246 **Tab. 1. Seismic velocities of the eclogites and granulites used for the FE calculations. The velocities**  
 247 **( $V_P$  and  $V_S$ ), densities and anisotropies were taken from Zertani et al. (2019a). The star indicates**  
 248 **that  $V_{PX}$  of N-101 was adjusted so that an anisotropy of 4% results (see text). Anisotropy was**  
 249 **calculated as  $100 \cdot (V_{PX} - V_{PY}) / V_{Pmean}$ . Velocities ( $V$ ) are given in  $\text{km s}^{-1}$ , density ( $\rho$ ) in  $\text{kg m}^{-3}$  and**  
 250 **anisotropy ( $A$ ) in %.**

Sample	eclogite		granulite	
	N-059	N-101	N-058A	N-103
$V_{PX}$	8.45	8.31*	7.12	7.76
$V_{PZ}$	7.74	8.01	6.99	7.46
$V_{S1}$	4.58	4.65	3.75	4.12
$V_{S2}$	4.70	4.64	3.77	4.24
$\rho$	3296	3483	2833	3139
$A_{VP}$	9	4	2	4



251

252

253

254

255

256

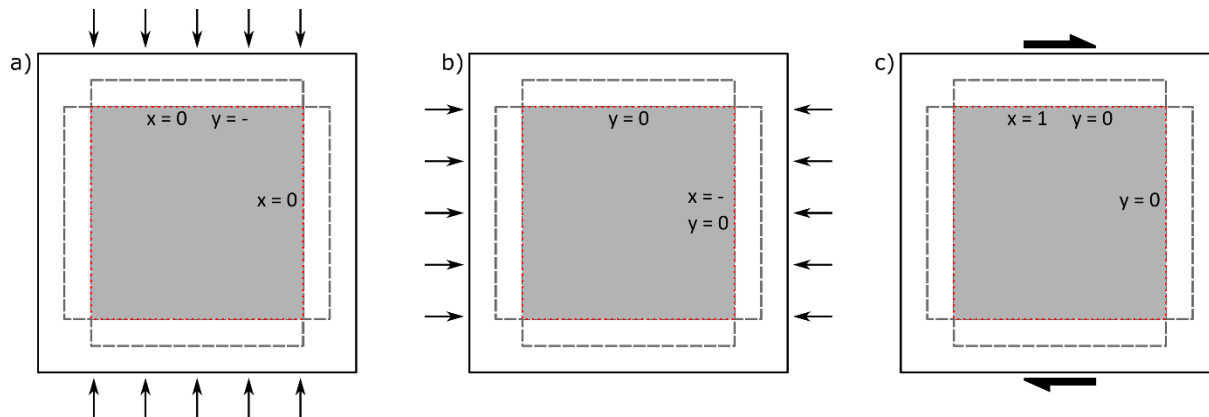
257

258

**Fig. 2. Examples of the geometries used for the FEM calculations. Eclogite is shown in green and granulite in white. (a) Small-scale eclogite facies shear zones representative of an area of ~20-by-20 m. The example shown here contains ~30% eclogite. For the calculations with other eclogite abundances the thickness of the shear zone was varied accordingly. (b) Small-scale static eclogite overprint representative of an area of ~20-by-20 m. The example shown here contains ~30% eclogite. For calculations with other eclogite abundances the size of the eclogite patches was varied accordingly. (c) Sheared eclogite breccia with regularly oriented granulite blocks. The example is**

259 representative of an area of ~100-by-100 m and ~70% eclogite. The size of the granulite blocks  
 260 remains the same throughout all calculations. To perform calculations with different eclogite  
 261 abundances the abundance of granulite blocks was altered. (d) Unsheared eclogite breccia with the  
 262 same variations as in (c). Below each image the corresponding properties of eclogite and granulite  
 263 used for the calculations are given. Each column represents one model series. The percentage gives  
 264 the strength of the P wave anisotropy of the corresponding rock and the arrow gives the orientation  
 265 of the fast P wave direction used for the calculations. L and H indicate whether the higher or lower-  
 266 anisotropy version was used.

267



268

269 **Fig. 3. Illustration of the three experiments with varying boundary conditions conducted for each**  
 270 **computation; (a) Vertical compression, (b) horizontal compression, and (c) horizontal simple shear.**  
 271 **The grey area represents the medium for which the properties are modelled. The red dotted square**  
 272 **represents the boundaries at which the results are extracted and the grey dashed lines represents**  
 273 **the area in which structures were extended if they are in direct contact with the boundary (see text**  
 274 **for details).**

275 **Tab. 2. Resulting minimum and maximum P wave velocities and P wave anisotropy for each of the**  
 276 **calculated models. Velocities are given in  $\text{km s}^{-1}$  and anisotropy is given in %. For each model the**  
 277 **properties of the granulite and eclogite used for the calculation is indicated with the following**  
 278 **scheme; L: low-anisotropy, H: high-anisotropy, X: fast axis is oriented horizontally, and Y: fast axis**  
 279 **is oriented vertically.**

280

Structural Association	Eclogite	Granulite	Vp <sub>min</sub>	Vp <sub>max</sub>	A	Vp <sub>min</sub>	Vp <sub>max</sub>	A	Vp <sub>min</sub>	Vp <sub>max</sub>	A	Vp <sub>min</sub>	Vp <sub>max</sub>	A	Vp <sub>min</sub>	Vp <sub>max</sub>	A
eclogite abundance [%]	H	X	H	X		7.51	7.91	5.2	7.54	7.97	5.7	7.56	8.04	6.1	7.58	8.10	6.6
	H	X	H	Y		7.66	7.75	1.2	7.70	7.77	1.0	7.72	7.86	1.8	7.74	7.95	2.7
	H	X	L	X		7.10	7.45	5.6	7.15	7.56	5.6	7.20	7.68	6.5	7.26	7.80	7.1
	H	X	L	Y		7.21	7.35	2.0	7.25	7.48	3.1	7.29	7.61	4.3	7.34	7.74	5.2
eclogite abundance [%]					10.9												
	L	X	H	X		7.55	7.85	4.0	7.60	7.91	4.1	7.62	7.94	4.2	7.67	8.00	4.2
	L	Y	H	X		7.59	7.80	2.7	7.67	7.82	1.9	7.72	7.84	1.6	7.79	7.86	0.9
	L	X	L	X		7.12	7.30	2.5	7.20	7.43	3.1	7.24	7.52	3.8	7.32	7.63	4.2
eclogite abundance [%]	L	Y	L	X		7.15	7.25	1.3	7.25	7.35	1.2	7.30	7.41	1.5	7.38	7.49	1.5
					53.1												
	H	X	H	X		7.64	8.20	7.1	7.67	8.27	7.6	7.69	8.32	7.9	7.71	8.37	8.3
	H	X	H	Y		7.75	7.99	3.0	7.75	8.19	5.6	7.74	8.26	6.5	7.74	8.34	7.4
Sheared eclogite breccia	H	X	L	X		7.45	7.96	6.7	7.53	8.10	7.3	7.58	8.19	7.8	7.65	8.30	8.2
	H	X	L	Y		7.50	7.91	5.3	7.57	8.06	6.4	7.61	8.17	7.1	7.66	8.28	7.7
					52.6												
	L	X	H	X		7.82	8.11	3.7	7.86	8.15	3.6	7.91	8.20	3.7	7.96	8.25	3.6
eclogite abundance [%]	L	X	H	Y		7.93	7.99	0.7	7.95	8.05	1.3	7.97	8.14	2.1	7.99	8.22	2.8
	L	X	L	X		7.63	7.83	2.5	7.72	7.92	2.5	7.81	8.05	3.0	7.91	8.16	3.2
	L	X	L	Y		7.60	7.65	0.6	7.68	7.77	1.1	7.76	7.87	1.4	7.84	8.01	2.2
					63.3												
Unsheared eclogite breccia	H	X	H	X		7.64	8.20	7.1	7.67	8.27	7.6	7.69	8.32	7.9	7.71	8.37	8.3
	H	X	H	Y		7.75	7.99	3.0	7.75	8.19	5.6	7.74	8.26	6.5	7.74	8.34	7.4
	H	X	L	X		7.45	7.96	6.7	7.53	8.10	7.3	7.58	8.19	7.8	7.65	8.30	8.2
	H	X	L	Y		7.50	7.91	5.3	7.57	8.06	6.4	7.61	8.17	7.1	7.66	8.28	7.7
eclogite abundance [%]					63.3												
	L	X	H	X		7.82	8.11	3.7	7.86	8.15	3.6	7.91	8.20	3.7	7.96	8.25	3.6
	L	X	H	Y		7.93	7.99	0.7	7.95	8.05	1.3	7.97	8.14	2.1	7.99	8.22	2.8
	L	X	L	X		7.63	7.83	2.5	7.72	7.92	2.5	7.81	8.05	3.0	7.91	8.16	3.2
Unsheared eclogite breccia	L	X	L	Y		7.60	7.65	0.6	7.68	7.77	1.1	7.76	7.87	1.4	7.84	8.01	2.2
					81.7												
	H	X	H	X		7.64	8.20	7.1	7.67	8.27	7.6	7.69	8.32	7.9	7.71	8.37	8.3
	H	X	H	Y		7.75	7.99	3.0	7.75	8.19	5.6	7.74	8.26	6.5	7.74	8.34	7.4
Sheared eclogite breccia	H	X	L	X		7.45	7.96	6.7	7.53	8.10	7.3	7.58	8.19	7.8	7.65	8.30	8.2
	H	X	L	Y		7.50	7.91	5.3	7.57	8.06	6.4	7.61	8.17	7.1	7.66	8.28	7.7
					81.7												
	L	X	H	X		7.82	8.11	3.7	7.86	8.15	3.6	7.91	8.20	3.7	7.96	8.25	3.6
Unsheared eclogite breccia	L	X	H	Y		7.93	7.99	0.7	7.95	8.05	1.3	7.97	8.14	2.1	7.99	8.22	2.8
	L	X	L	X		7.63	7.83	2.5	7.72	7.92	2.5	7.81	8.05	3.0	7.91	8.16	3.2
	L	X	L	Y		7.60	7.65	0.6	7.68	7.77	1.1	7.76	7.87	1.4	7.84	8.01	2.2
					90.3												

## 282 **4. Results**

283 In order to approximate bulk P wave velocities and anisotropy of the structural associations on  
284 Holsnøy we calculate the properties of the effective medium of exemplary geometries with  
285 varying attributes (Fig. 2). These geometries are constructed based on field observations from  
286 Zertani et al. (2019b). The panels in Fig. 2 correspond to each of the endmembers distinguished  
287 in Zertani et al. (2019b). We then systematically vary the main configurations that can be  
288 observed in the field. These are: a) amount of eclogites, b) orientation of the main foliation or the  
289 constituting lithologies, and c) strength of the deformation fabric in the individual lithologies,  
290 mainly considering if the eclogites were dominated by static or dynamic eclogitization.  
291 Granulites with small-scale shear zones and granulites with small-scale static eclogitization  
292 features are each calculated with eclogite abundances between ~10 and ~50% and the sheared  
293 and unsheared eclogite breccia are calculated with eclogite abundances between ~50 and ~90%.  
294 Additionally, the orientation of the fast and slow axis of granulites and eclogites is varied so that  
295 the anisotropy of the constituting lithologies is either parallel or perpendicular to each other. Fig.  
296 2 and Tab. 2 summarize the orientations used for each calculation as well as the rock properties of  
297 the eclogites and granulites implemented in the models.

### 298 4.1 P wave velocity and anisotropy of small-scale eclogitization features

299 The process of eclogitization, as it can be studied on Holsnøy, is driven by two contrasting  
300 endmember mechanisms: eclogitization proceeding along shear zones (Fig. 2a) or developing as a  
301 static overprint (Fig. 2b). In the first type, eclogitization proceeds along shear zones that widen  
302 progressively with time (Austrheim, 1987). Thus, we calculated P wave velocities for 20  
303 examples with varying shear zone thickness as well as varying elastic properties of the eclogite  
304 and granulite implemented in the models (see Fig. 2, Tab. 2 for details).

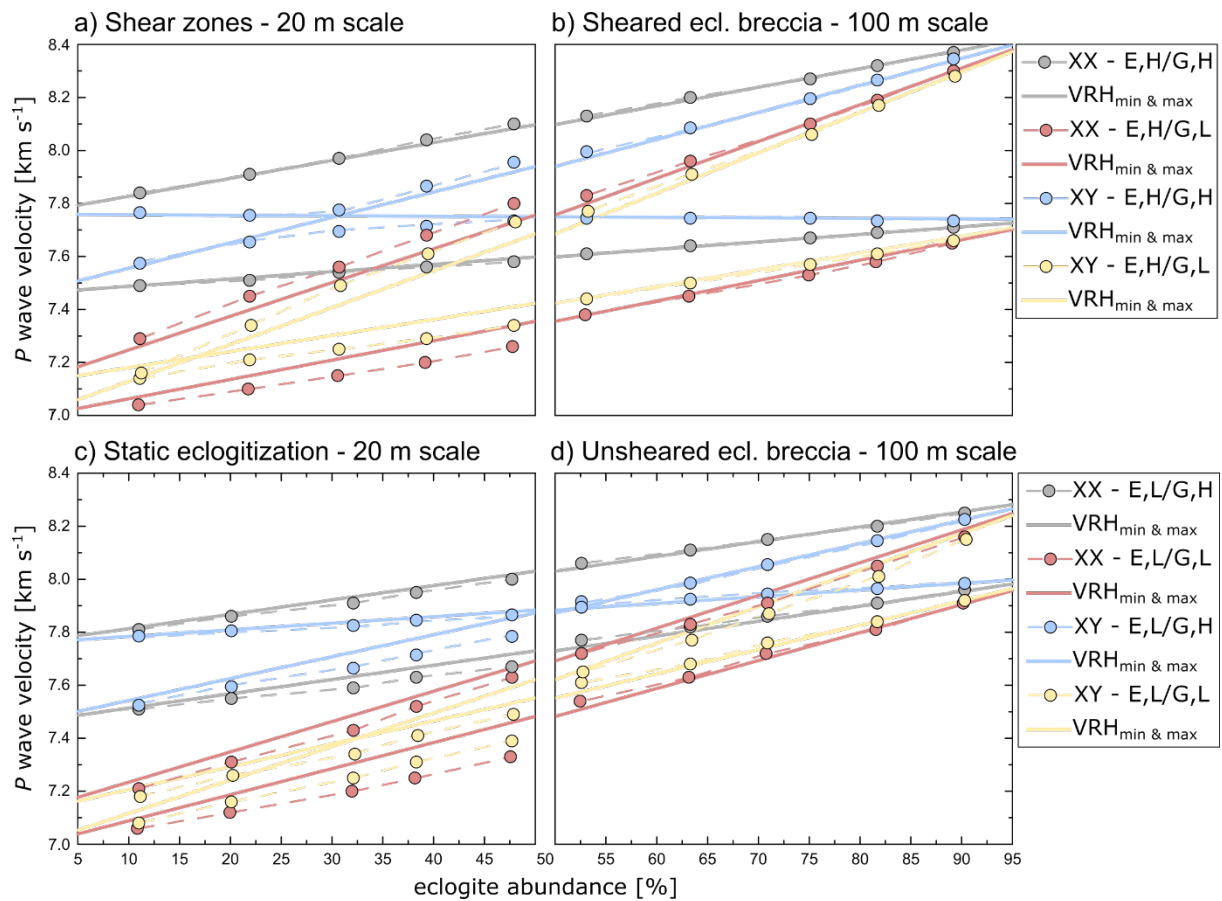
305 Comparing all models shows that the calculated P wave velocities with higher-anisotropy  
306 (stronger deformation fabric) granulites are, in general, higher than those with lower-anisotropy  
307 granulites. Furthermore, with increasing shear zone thickness (i.e., amount of eclogite), the P  
308 wave velocity in both the slow and the fast P wave direction increases linearly (Tab. 2; Fig. 4a).  
309 The one exception to this trend is given by the models that feature both higher-anisotropy  
310 eclogite and the higher-anisotropy granulite, with the fast axis of both rocks oriented  
311 perpendicular to each other: the fast axis of the eclogite parallel to the shear zones and the fast  
312 axis of the granulite perpendicular to them. For this geometry, the resulting P wave velocities for  
313 the fast and slow axis of the effective medium converge up to an eclogite abundance of ~30%  
314 and then diverge toward higher eclogite abundance. This coincides with a change of the  
315 orientations of the fast and slow direction. In this scenario, the velocity perpendicular to the  
316 shear zones is almost constant. The velocity parallel to the shear zones, however, increases  
317 significantly from 7.58 to 7.95 km s<sup>-1</sup> with increasing eclogite abundance. The fast axis is thus  
318 perpendicular to the shear zones for an eclogite abundance <30% and parallel to the shear zones  
319 from ~30–50% eclogite abundance. The orientation of the slow direction rotates progressively in  
320 the other direction. In all other model sequences, the fast direction is parallel to the shear zones  
321 and the slow direction is perpendicular.

322 The corresponding P wave anisotropy also increases with increasing shear zone thickness and  
323 reaches a maximum value of 7.1% (Fig. 5). In most models, this increase is near-linear with  
324 increasing eclogite abundance. In contrast, the resulting P wave anisotropy of those calculations  
325 featuring a higher-anisotropy granulite with the fast axis oriented perpendicular to the shear zone  
326 decreases between ~10% and ~30% eclogite abundance and then increases until ~50% eclogite



327 abundance. Finally, the P wave anisotropy at ~50% eclogite abundance returns to approximately  
 328 the same value of ~2-3%, as the P wave anisotropy at ~10% eclogite abundance.

329 In general, the resulting P wave anisotropy is larger when the fast axes of both granulite and  
 330 eclogite are oriented parallel to the shear zone, compared to those examples where the fast axis  
 331 of the granulite is oriented perpendicular to the shear zone. At lower eclogite abundance the  
 332 calculations implementing a higher-anisotropy granulite result in a higher anisotropy of the  
 333 effective medium, while the results at higher eclogite abundance indicate that the anisotropy of  
 334 the effective medium is higher if the granulite has a lower intrinsic anisotropy (Fig. 5).

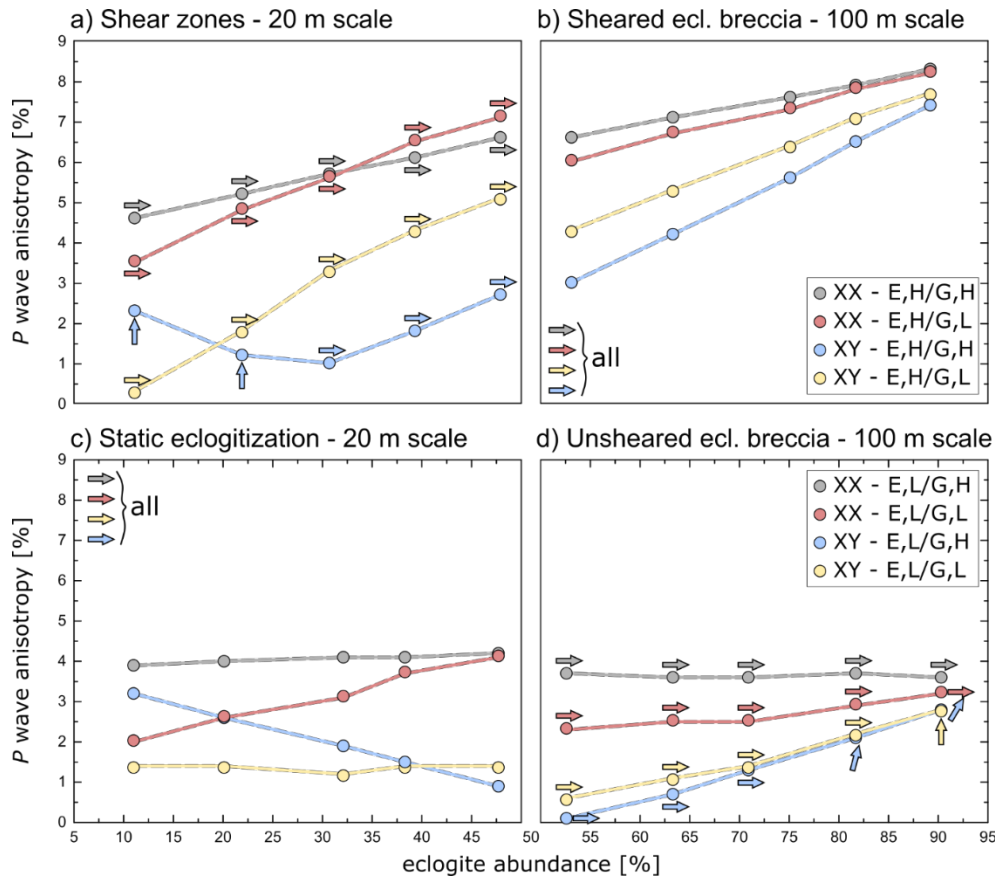


335

336 **Fig. 4. P wave velocities of the FEM calculations: (a) Small-scale eclogite shear zones, (b) sheared**  
 337 **eclogite breccia, (c) small-scale static eclogite, and (d) unsheared eclogite breccia. The legend for (a)**  
 338 **and (b) is to the right of (b) and the legend for (c) and (d) is to the right of (d). Each model series is**  
 339 **shown by two connecting dashed lines. The upper line represents the maximum velocities and the**  
 340 **lower line represents the minimum velocities. The legend is given in the following scheme; XX: fast**  
 341 **axis of granulite and eclogite are parallel, XY: fast axis of granulite and eclogite are perpendicular,**

342 E,H or E,L: eclogite with high anisotropy or low anisotropy, respectively, G,H or G,L: granulite  
 343 with high or low anisotropy, respectively. Solid lines indicate Voigt-Reuss-Hill averages in the same  
 344 color scheme as the modeling results averaged from the input velocities in x and y direction,  
 345 respectively, thus giving minimum and maximum bounds.

346



347

348 **Fig. 5. P wave anisotropy of the FEM calculations: (a) Small-scale eclogite shear zones, (b) sheared**  
 349 **eclogite breccia, (c) small-scale static eclogite, and (d) unsheared eclogite breccia. For a description**  
 350 **of model types and explanation of the legend, refer to Fig. 4. Arrows indicate the direction of the**  
 351 **fast axis of the effective medium with horizontal being in x direction and vertical in y direction.**

352

353 Additionally, eclogitization on Holsnøy also proceeded statically without significant ductile

354 deformation (Jamtveit et al., 2000; Zertani et al., 2019b). Here, eclogitization most commonly

355 advances parallel to the granulite foliation. For this case, we again calculated 20 different

356 examples, varying both the abundance of eclogite and the elastic properties of the granulite and

357 the eclogite (Fig. 2b; Tab. 2).

358 The resulting P wave velocities show a similar trend as those from the examples featuring small-  
359 scale shear zones. Both the velocity of the fast and the slow axes increase linearly with  
360 increasing abundance of eclogite (Fig. 4c). Further, the models featuring granulites with higher  
361 anisotropy result in faster P wave velocities of the effective medium than the models  
362 implementing lower-anisotropy granulites. Additionally, the P wave velocities are in the same  
363 range as the ones calculated for small-scale shear zones.

364 The orientations of the fast and slow axes are typically constant with the fast axis being parallel  
365 to the granulite foliation (horizontal) and the slow axis perpendicular. Only in the calculations  
366 where the lower-anisotropy eclogite and granulite with the orientation of the fast axes  
367 perpendicular to each other are implemented, the resulting orientation changes slightly. These  
368 calculations indicate that the fast axis remains horizontal (i.e., parallel to the granulite foliation)  
369 while the slow axis rotates slightly away from the initial vertical orientation.

370 The P wave anisotropy shows a variable trend comparing the different models. The medium  
371 featuring the higher-anisotropy granulite, with both the fast axes of the granulite and eclogite  
372 oriented parallel to each other result in a P wave anisotropy of ~4% that essentially does not  
373 change with varying eclogite abundance (Fig. 5d). The same is observed for the models featuring  
374 the lower-anisotropy granulite with the fast axes of the granulite and eclogite being oriented  
375 perpendicular to each other. Here, the resulting P wave velocity remains relatively constant  
376 around 1–2%.

377 In contrast, the resulting anisotropy of the other two model types changes with increasing  
378 eclogite abundance. The sequence featuring a lower-anisotropy granulite with the fast axis  
379 oriented parallel to the fast axis of the eclogite increases from ~2% to ~4%, while the sequence

380 featuring the higher-anisotropy granulite with the fast axes of the two rocks oriented  
381 perpendicular to each other decreases from ~3% to <1%.

#### 382 4.2 P-wave velocity of eclogite breccia

383 With increasing degree of eclogitization the so-called eclogite breccia develops, which is  
384 composed of an eclogite matrix that surrounds preserved blocks of granulite (Boundy et al.,  
385 1992). On Holsnøy, the eclogite breccia can be divided into two endmember types (Zertani et al.,  
386 2019b): The sheared eclogite breccia is characterized by a strongly sheared and foliated eclogite  
387 matrix, while the matrix of the unsheared eclogite breccia is diffuse and less foliated.

388 We calculated 20 examples for each of the two types, varying the abundance of eclogite and the  
389 elastic properties of the granulite and eclogite (see Fig. 2c, d; Tab. 2). For all examples of the  
390 sheared eclogite breccia, the P wave velocities increase linearly with increasing eclogite  
391 abundance. All fast axes and all slow axes converge toward higher eclogite abundances, thus  
392 giving fairly distinct maximum and minimum P wave velocities at high eclogite abundances that  
393 are independent of the elastic properties of the granulite implemented in the model. (Fig. 4; Fig. 5).  
394 The slope of the linear increase for the different models is similar to the models dealing with  
395 small-scale shear zones. Further, the fast axis of the effective medium in all models is parallel to  
396 the shear plane (horizontal) and the slow axis is perpendicular. Additionally, the P wave  
397 velocities at ~50% eclogite abundance agree well between the models for small-scale shear zones  
398 and the sheared eclogite breccia at the same eclogite fraction.

399 As in the case of the small-scale shear zones, the P wave anisotropy calculated for the sheared  
400 eclogite breccia increases nearly linearly with increasing eclogite abundance reaching 7–9% at  
401 ~90%. Further, P wave anisotropy is consistently higher for models where the fast axes of the  
402 granulite and the eclogite are oriented parallel. In this scenario the anisotropy reaches its

403 maximum when both the granulite and the eclogite have a high anisotropy. If the fast axis of the  
404 granulite, however, is perpendicular to the fast axis of the eclogite, the resulting anisotropy is  
405 higher when the implemented granulite has a lower anisotropy.

406 The P wave velocities calculated for the unsheared eclogite breccia show the same general trends  
407 as those for the sheared eclogite breccia (Fig. 4d). The only deviation results from the examples  
408 implementing granulite and eclogite with their anisotropy perpendicular to each other. Here the  
409 calculations result in a change of the orientation at high eclogite abundances.

410 The trends of the P wave anisotropy of the unsheared eclogite breccia in all calculated examples  
411 is lower than the comparable examples of the sheared eclogite breccia (Fig. 5). Most sequences,  
412 however, also slightly increase with increasing eclogite abundance, except for those where a  
413 lower-anisotropy eclogite is paired with the higher-anisotropy granulite, both of which have their  
414 fast axes parallel to each other. In that case the P wave anisotropy is nearly constant at ~3.7%  
415 (Tab. 2).

## 416 **5. Discussion**

417 Many studies have calculated or measured P wave velocities of various metamorphic rocks with  
418 the aim of interpreting the results of large-scale geophysical imaging techniques (e.g., Almquist  
419 & Mainprice, 2017). However, the sample sizes used for these interpretations are typically far  
420 below the resolution of geophysical studies. It is thus essential to understand how geometries  
421 formed at depth during ongoing eclogitization shape the seismic properties of the effective  
422 medium in combination with the (anisotropic) seismic properties of the constituent rocks.

### 423 5.1 Effective properties of 20 m and 100 m scale structures

424 Essentially, the P wave velocities calculated for the different geometrical setups show that the  
425 velocities are controlled by the velocities of the constituent rocks and their proportions (Fig. 4,

426 Fig. 5). This has been accepted and applied by previous studies by calculating, for example,  
427 Voigt-Reuss-Hill (VRH) averages (Hill, 1952) and linking those with the crystallographic  
428 preferred orientations of the mineral phases (e.g., Hacker et al., 2014; Llana-Funez & Brown,  
429 2012; Worthington et al., 2013). Most of these studies, however, obtain information from the  
430 thin section scale to recognize crustal-scale processes or to interpret the results from large-scale  
431 geophysical imaging studies. The results presented in this study indicate that Voigt-Reuss-Hill  
432 averages calculated from outcrop-scale features are sufficiently precise to estimate the effective  
433 properties on a variety of scales (Fig. 4). Essentially, the geometries that are representative of  
434 eclogitization of crustal rocks have only limited influence on the resulting P wave velocities.  
435 Only in isolated cases the velocities are modified, thus deviating from the calculated VRH  
436 averages (Fig. 4a and 4c). Here a minor geometric effect is plausible, however, this effect results  
437 in a maximum modification of  $<0.2 \text{ km s}^{-1}$  of the P wave velocity and is thus negligible in the  
438 context of large-scale crustal processes.

439 However, P wave anisotropy varies between the different geometrical configurations (Fig. 5).  
440 Here, we distinguish two contributing factors in order to characterize their influence separately.  
441 (1) The configuration that the different lithologies have to one another on the outcrop scale or  
442 larger. This includes, for example, eclogite shear zones that crosscut granulites. In the following  
443 this factor will be termed external geometry as it involves the relationship of the lithologies to  
444 each other but not specifically the properties of the constituting lithologies themselves. (2) The  
445 second contributing geometrical factor will be termed internal geometry in the following. It  
446 highlights the properties of the lithologies themselves by characterizing the relationship between  
447 the directional dependence of the elastic properties of the different lithologies that is caused by,  
448 for example, crystallographic preferred orientations or shape preferred orientations. The internal

449 geometry thus distinguishes whether the fastest velocity of the eclogite and granulite are parallel  
450 or oblique to each other.

451 Our results reveal the importance of the internal geometry compared to that of the external  
452 geometry (Fig. 4, Fig. 5). As discussed above, the external geometry only has a minor effect on  
453 the P wave velocities and anisotropy of the effective medium. The variation of anisotropy for the  
454 different configurations tested by us are thus controlled by the internal geometry. The most  
455 important factor is the anisotropy of the constituent lithologies that are necessary to produce  
456 significant anisotropy of the effective medium. Additionally, the effective anisotropy is  
457 strengthened or weakened by the relationship of the individual anisotropies of the lithologies.  
458 Anisotropies are higher if the fast axes of the lithologies are aligned but not higher than the  
459 highest contributing anisotropy (Fig. 5). Further, our results demonstrate the predominance of the  
460 higher anisotropy lithology and suggest that the fast axis of the effective medium is parallel to  
461 the anisotropy of the matrix lithology (i.e., in line with the fabric of granulite or eclogite), if the  
462 difference in anisotropy between the lithologies is small, or the higher anisotropy lithology, even  
463 if this lithology is less abundant (Fig. 5); meaning a strongly deformed rock, such as eclogite in  
464 shear zones, controls the overall anisotropy even at low abundances.

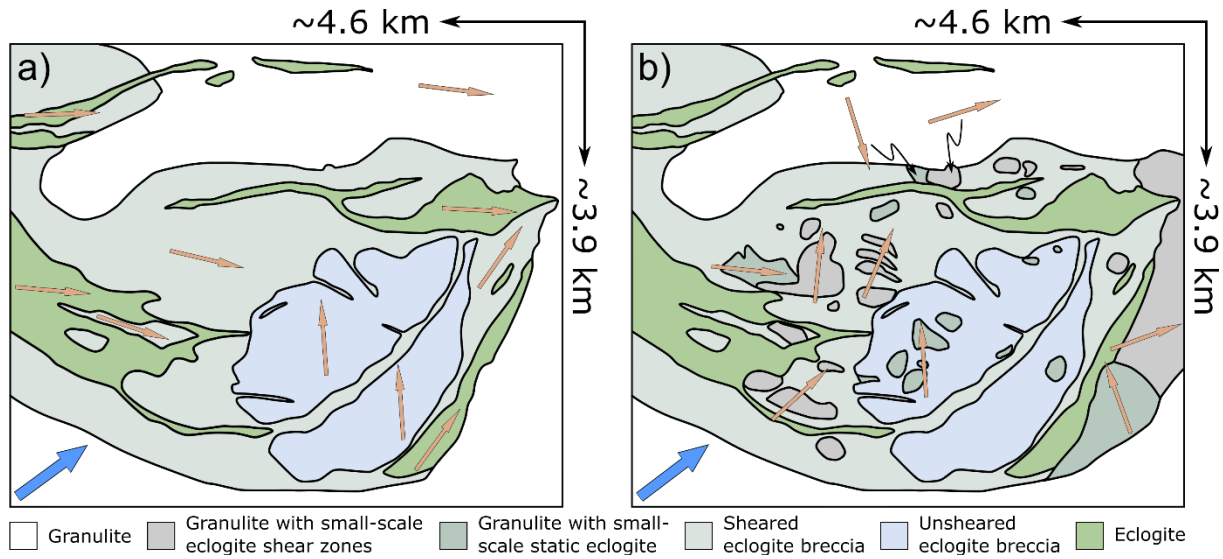
## 465 5.2 Effective properties on the kilometer scale

466 Combining our results with field observations provides the opportunity to understand how partial  
467 eclogitization of crustal rocks alters the seismic properties on a scale significantly larger than  
468 what can be measured in the laboratory. Our results suggest that P wave velocities are almost  
469 entirely controlled by the velocities and abundances of the constituting rocks (Fig. 4). Essentially,  
470 there is no difference in the P wave velocities between rocks that have formed through static  
471 eclogitization and those that formed associated with ductile deformation. Neither the finite

472 geometries nor the intrinsic seismic anisotropy of the granulites and eclogites have a significant  
473 impact on the resulting bulk velocities and the variations that can be distinguished are minor. The  
474 P wave anisotropy, however, is influenced strongly by the anisotropy of the rocks that make up  
475 the effective medium (Fig. 5). Further, our results show that the rock with the higher anisotropy  
476 controls bulk anisotropy. In any case, the exemplary geometries discussed above are still far  
477 smaller than what can be resolved with large-scale geophysical methods.

478 Therefore, we used these results to extract bulk properties of the effective medium at a scale that  
479 could be resolved by large-scale geophysical imaging (Fig. 6). Accordingly, we used an area on  
480 Holsnøy that is ~3.9-by-4.6 km in size (Fig. 1 and Fig. 6a), and provides a coherent natural  
481 laboratory for eclogitization related structures. The geometries are based on the map shown in  
482 Zertani et al. (2019b). As properties for the different map units we implemented the resulting  
483 elastic tensor of the examples shown above, choosing one representative example for each of the  
484 geometric configurations, i.e., sheared eclogite breccia at ~75% eclogite with the fast axis of  
485 higher-anisotropy eclogite and higher-anisotropy granulite parallel to each other and unsheared  
486 eclogite breccia at ~71% eclogite with the fast axis of the lower-anisotropy eclogite and the  
487 higher-anisotropy granulite parallel to each other (Tab. 2). For pure eclogite and granulite we  
488 chose the higher-anisotropy versions (Tab. 1) that were also used for the calculations discussed  
489 above (Zertani et al., 2019a). The elastic tensors were rotated so that the fast axis is parallel to  
490 the structures presented by Zertani et al. (2019b).





491  
 492 **Fig. 6. Geometries used for the FEM calculations on the kilometer-scale. (a) Simpler model without**  
 493 **smaller-scale structures. (b) More realistic model with small-scale structures. The location of this**  
 494 **figure is given in Fig. 1. The yellow arrows indicate the direction of the fast axis implemented for**  
 495 **the different lithologies. The blue arrows show the direction of the fastest velocity for each of the**  
 496 **models.**

497  
 498 Additionally, we implemented a second (more precise) model that also includes smaller-scale  
 499 structures (Fig. 6b). Here we implemented the small-scale eclogite shear zones at ~31% eclogite  
 500 with the lower-anisotropy granulite and the higher-anisotropy eclogite (Tab. 2) and the small-  
 501 scale static eclogite occurrences at ~32% eclogite with the higher-anisotropy granulite and the  
 502 lower-anisotropy eclogite (Tab. 2).

503 The resulting P wave velocities of both models are in the range of  $8.1 \text{ km s}^{-1}$  (fast axis) to  $7.7 \text{ km}$   
 504  $\text{s}^{-1}$  (slow axis), i.e., within the expected range of the measured P wave velocities between  
 505 granulite and eclogite (Zertani et al., 2019a). Similar velocities are also reported from  
 506 geophysical studies dealing with active convergent settings, typically in the range of  $7\text{--}8 \text{ km s}^{-1}$   
 507 (e.g., Nabelek et al., 2009; Schulte-Pelkum et al., 2005; Sippl et al., 2013). Additionally, our  
 508 calculation predicts a P wave anisotropy of 5.1% for the simpler model (Fig. 6a) and 4.8% for the  
 509 model that includes the small-scale structures (Fig. 6b). These values are in the range of what is  
 510 generally reported from higher-anisotropy eclogites and granulites (e.g., Brown et al., 2009;

511 Worthington et al., 2013). However, it has to be noted that the anisotropy presented here is  
512 representative for the effective medium on a kilometer-scale and not only for single  
513 (handspecimen-sized) samples.

### 514 5.3 Implications for imaging of continental collision

515 P wave velocities below the Tibetan plateau are suggested to be  $>7.0 \text{ km s}^{-1}$ , which was  
516 interpreted to represent  $\sim 30\%$  eclogitization (Schulte-Pelkum et al., 2005). Our calculation for  
517 Holsnøy is representative of  $\sim 50\%$  eclogitization and yields slightly higher velocities. It thus  
518 seems possible to estimate the degree of eclogitization based on P wave velocities. However, this  
519 is only feasible if the backazimuthal distribution is sufficiently representative (Nabelek et al.,  
520 2009; Schulte-Pelkum et al., 2005).

521 The retrieved P wave anisotropy of  $\sim 5\%$  from our model is sufficiently high that it could result  
522 in a backazimuthal dependence of the retrieved signal in seismological studies. Additionally, our  
523 calculations of P wave anisotropy of the different structural associations that could be expected  
524 in a partially eclogitized crust show how different geometries can cause high P-wave anisotropy  
525 (Fig. 5). A typical example of an active setting where the rocks at depth are presumably similar to  
526 those on Holsnøy is the Himalaya-Tibet collision system, where the lower crust of India is  
527 imaged below the Himalaya (Jackson et al., 2004; Labrousse et al., 2010). Using the receiver  
528 function method, it has been shown that the retrieved signal of the Moho is sharp using  
529 earthquakes coming from the north, while the Moho cannot be clearly imaged using earthquakes  
530 arriving from the south, suggesting an anisotropic fabric within the buried crust (Nabelek et al.,  
531 2009; Schulte-Pelkum et al., 2005). Nabelek et al. (2009) propose that this fabric is caused by the  
532 imbrication and rotation of a stratified lower crust, excluding eclogites as the cause for the  
533 anisotropy because eclogites typically have anisotropies  $<4\%$ . However, our results show that

534 partial eclogitization of the lower crust does indeed produce high anisotropies at the scale  
535 sampled by geophysical imaging techniques. Moreover, as shown by our results the effect of  
536 external geometry on seismic anisotropy is limited suggesting that simple layering or imbrication  
537 might not produce sufficient seismic anisotropy on this scale. Our results provide an alternative  
538 explanation for the structures observed below the Himalaya. We suggest that considering the P  
539 wave velocities reported and the backazimuthal dependence (Nabelek et al., 2009; Schulte-  
540 Pelkum et al., 2005) eclogitization of the crust along ductile shear zones, similar to those  
541 exposed on Holsnøy seems the more likely explanation.

542 Additionally, both kilometer-scale models we present here suggest that the fast axis of the shear  
543 zone system is oriented WSW-ENE. At least in a qualitative sense this suggests that during  
544 ongoing eclogitization, when this anisotropy was established it was dipping toward the upper  
545 plate as is also evidenced by the top-east kinematics of the shear zone system (Jolivet et al.,  
546 2005; Raimbourg et al., 2005). Geophysical imaging suggests a northward dipping fabric within  
547 the lower Indian crust (Nabelek et al., 2009; Schulte-Pelkum et al., 2005), that is, dipping toward  
548 the Asian plate, consistent with a top to the south shear sense. Our results demonstrate that  
549 propagating eclogite-facies shear zones would produce a fabric and subsequent anisotropy with a  
550 similar orientation. The scale of those shear zones is actually a minor issue, since our results  
551 show the same dependence of effective medium properties on constitutive lithologies  
552 independent of the scale.

553

#### 554 5.4 Implications for oceanic subduction

555 Although the rocks on Holsnøy originate from continental crust some implications for oceanic  
556 subduction settings can nevertheless be explored. In many geophysical studies of subducting

557 oceanic plates the descending crust is clearly imaged at shallow depth but loses its seismic signal  
558 at greater depth (e.g., Bostock et al., 2002; Pearce et al., 2012; Rondenay et al., 2008; Yuan et  
559 al., 2000). This decrease of the seismic signal is typically interpreted as due to a decreased  
560 impedance contrast between descending crust and mantle rocks caused by eclogitization. This is  
561 often accompanied by an increase of the dip angle in the Wadati-Benioff zone that indicates a  
562 kink in the slab geometry (e.g., Halpaap et al., 2018; Klemd et al., 2011; Yuan et al., 2000).  
563 While the subducting crust is invisible to seismological studies at this point its presence is  
564 evidenced by the Wadati-Benioff zone and the inferred kink of the slab has been proposed as a  
565 possible geometric obstacle that inhibits exhumation of crustal material subducted beyond that  
566 point and is therefore potentially vital to understand subduction zone processes (Klemd et al.,  
567 2011). Additionally, kinking on this scale must cause internal deformation of the subducting  
568 slab. Whether or not this deformation is localized or homogeneously distributed and how this  
569 deformation process affects ongoing eclogitization of the slab is enigmatic. However, utilizing  
570 seismic anisotropy and the subsequent backazimuthal bias on the retrieved seismic signal might  
571 prove a powerful tool to unravel these processes in active subduction zones. In this context,  
572 although reliable imaging of the crustal anisotropy at these depths is still challenging, seismic  
573 anisotropy of the subducted oceanic crust might make it possible to image it to larger depth and  
574 illuminate an otherwise invisible slab.

575

## 576 **6. Conclusions**

577 We calculated P wave velocities and the corresponding P wave anisotropy for various  
578 geometries, which are representative of partially eclogitized crust. The results show that dynamic  
579 eclogitization, associated with shear zone formation, can cause a high P wave anisotropy that

580 increases with increasing eclogitization. The anisotropy of the effective medium is generally  
581 controlled by the anisotropy of the matrix or by the contributing lithology that has the highest  
582 anisotropy, even if this lithology is less abundant than the other contributors. Consequently,  
583 patches of static eclogitization produce a comparatively low P wave anisotropy, which is in some  
584 cases independent of the amount of eclogitization. The (external) geometric configuration of the  
585 lithologies has little to no effect on the seismic properties of the effective medium.  
586 Our results link partial eclogitization with geophysical observations at active convergent plate  
587 boundaries. Previously, significant anisotropy due to eclogitization in deeply buried or subducted  
588 crust has been excluded as eclogites are typically not strongly anisotropic. Contrary to this, our  
589 results demonstrate that significant anisotropy due to partial eclogitization of crustal material on  
590 a kilometer-scale is likely the best explanation for the discrepancy of the signals retrieved from  
591 different backazimuths in seismological studies. For example, the structures seen below the  
592 Himalaya are likely anisotropic due to the formation of eclogite-facies shear zones within the  
593 lower Indian crust. Additionally, our results strongly encourage the utilization of seismic  
594 anisotropy as a tool to visualize the structural associations at depth thus aiding the extraction of  
595 the underlying mechanisms active during ongoing eclogitization of crustal material.

596

#### 597 Acknowledgements

598 This research was supported by the Deutsche Forschungsgemeinschaft (DFG) in the framework  
599 of the priority program SPP 2017 “Mountain Building in Four Dimensions (MB-4D)” by grant  
600 JO 349/11-1. Funding for TBA was provided from Norges forskningsråd (NFR) project 250327.  
601 Input data for the calculations are provided as figures in the supporting information and will be  
602 uploaded to the OSF data repository ([osf.io](https://osf.io)) after acceptance.

603

## 604 References

605

606

607 Almqvist, B. S. G., & Mainprice, D. (2017). Seismic properties and anisotropy of the continental  
608 crust: Predictions based on mineral texture and rock microstructure. *Reviews of*  
609 *Geophysics*, 55(2), 367-433. doi:<https://doi.org/10.1002/2016RG000552>

610 Andersen, T. B., Corfu, F., Labrousse, L., & Osmundsen, P.-T. (2012). Evidence for  
611 hyperextension along the pre-Caledonian margin of Baltica. *Journal of the Geological*  
612 *Society*, 169(5), 601-612. doi:<https://doi.org/10.1144/0016-76492012-011>

613 Austrheim, H. (1987). Eclogitization of lower crustal granulites by fluid migration through shear  
614 zones. *Earth and Planetary Science Letters*, 81(2), 221-232.  
615 doi:[https://doi.org/10.1016/0012-821X\(87\)90158-0](https://doi.org/10.1016/0012-821X(87)90158-0)

616 Austrheim, H. (1990). The granulite-eclogite facies transition: A comparison of experimental  
617 work and a natural occurrence in the Bergen Arcs, western Norway. *Lithos*, 25(1), 163-  
618 169. doi:[https://doi.org/10.1016/0024-4937\(90\)90012-P](https://doi.org/10.1016/0024-4937(90)90012-P)

619 Austrheim, H. (1991). Eclogite formation and dynamics of crustal roots under continental  
620 collision zones. *Terra Nova*, 3(5), 492-499. doi:[https://doi.org/10.1111/j.1365-  
621 3121.1991.tb00184.x](https://doi.org/10.1111/j.1365-3121.1991.tb00184.x)

622 Austrheim, H., & Griffin, W. L. (1985). Shear deformation and eclogite formation within  
623 granulite-facies anorthosites of the Bergen Arcs, western Norway. *Chemical Geology*,  
624 50(1), 267-281. doi:[https://doi.org/10.1016/0009-2541\(85\)90124-X](https://doi.org/10.1016/0009-2541(85)90124-X)

625 Backus, G. E. (1962). Long-wave elastic anisotropy produced by horizontal layering. *Journal of*  
626 *Geophysical Research*, 67(11), 4427-4440. doi:10.1029/JZ067i011p04427

627 Bhowany, K., Hand, M., Clark, C., Kelsey, D. E., Reddy, S. M., Pearce, M. A., . . . Morrissey, L.  
628 J. (2018). Phase equilibria modelling constraints on P–T conditions during fluid catalysed  
629 conversion of granulite to eclogite in the Bergen Arcs, Norway. *Journal of Metamorphic*  
630 *Geology*, 36(3), 315-342. doi:<https://doi.org/10.1111/jmg.12294>

631 Bloch, W., John, T., Kummerow, J., Salazar, P., Krüger, O. S., & Shapiro, S. A. (2018).  
632 Watching Dehydration: Seismic Indication for Transient Fluid Pathways in the Oceanic  
633 Mantle of the Subducting Nazca Slab. *Geochemistry, Geophysics, Geosystems*, 19, 3189-  
634 3207. doi:<https://doi.org/10.1029/2018GC007703>

635 Bostock, M., Hyndman, R., Rondenay, S., & Peacock, S. (2002). An inverted continental Moho  
636 and serpentinization of the forearc mantle. *Nature*, 417, 536-538.  
637 doi:<https://doi.org/10.1038/417536a>

638 Bostock, M. G. (2013). The Moho in subduction zones. *Tectonophysics*, 609, 547-557.  
639 doi:<https://doi.org/10.1016/j.tecto.2012.07.007>

640 Boundy, T. M., Fountain, D. M., & Austrheim, H. (1992). Structural development and  
641 petrofabrics of eclogite facies shear zones, Bergen Arcs, western Norway: implications  
642 for deep crustal deformational processes. *Journal of Metamorphic Geology*, 10(2), 127-  
643 146. doi:<https://doi.org/10.1111/j.1525-1314.1992.tb00075.x>

644 Boundy, T. M., Mezger, K., & Essene, E. J. (1997). Temporal and tectonic evolution of the  
645 granulite-eclogite association from the Bergen Arcs, western Norway. *Lithos*, 39(3), 159-  
646 178. doi:[http://dx.doi.org/10.1016/S0024-4937\(96\)00026-6](http://dx.doi.org/10.1016/S0024-4937(96)00026-6)

- 647 Brown, D., Llana-Funez, S., Carbonell, R., Alvarez-Marron, J., Marti, D., & Salisbury, M.  
648 (2009). Laboratory measurements of P-wave and S-wave velocities across a surface  
649 analog of the continental crust–mantle boundary: Cabo Ortegal, Spain. *Earth and*  
650 *Planetary Science Letters*, 285(1-2), 27-38. doi:<https://doi.org/10.1016/j.epsl.2009.05.032>
- 651 Corfu, F., Andersen, T. B., & Gasser, D. (2014). The Scandinavian Caledonides: main features,  
652 conceptual advances and critical questions. *Geological Society, London, Special*  
653 *Publications*, 390(1), 9-43. doi:<https://doi.org/10.1144/sp390.25>
- 654 Dewey, J. F., Ryan, P. D., & Andersen, T. B. (1993). Orogenic uplift and collapse, crustal  
655 thickness, fabrics and metamorphic phase changes: the role of eclogites. *Geological*  
656 *Society, London, Special Publications*, 76(1), 325-343.  
657 doi:<https://doi.org/10.1144/GSL.SP.1993.076.01.16>
- 658 Fountain, D. M., Boundy, T. M., Austrheim, H., & Rey, P. (1994). Eclogite-facies shear zones—  
659 deep crustal reflectors? *Tectonophysics*, 232(1), 411-424.  
660 doi:[https://doi.org/10.1016/0040-1951\(94\)90100-7](https://doi.org/10.1016/0040-1951(94)90100-7)
- 661 Glodny, J., Kühn, A., & Austrheim, H. (2008). Geochronology of fluid-induced eclogite and  
662 amphibolite facies metamorphic reactions in a subduction–collision system, Bergen Arcs,  
663 Norway. *Contributions to Mineralogy and Petrology*, 156(1), 27-48.  
664 doi:<https://doi.org/10.1007/s00410-007-0272-y>
- 665 Hacker, B., Ritzwoller, M., & Xie, J. (2014). Partially melted, mica-bearing crust in Central  
666 Tibet. *Tectonics*, 33(7), 1408-1424. doi:<https://doi.org/10.1002/2014TC003545>
- 667 Halpaap, F., Rondenay, S., & Ottemöller, L. (2018). Seismicity, Deformation, and  
668 Metamorphism in the Western Hellenic Subduction Zone: New Constraints From  
669 Tomography. *Journal of Geophysical Research: Solid Earth*, 123(4), 3000-3026.  
670 doi:<https://doi.org/10.1002/2017JB015154>
- 671 Hetényi, G., Cattin, R., Brunet, F., Bollinger, L., Vergne, J., Nábělek, J. L., & Diament, M.  
672 (2007). Density distribution of the India plate beneath the Tibetan plateau: Geophysical  
673 and petrological constraints on the kinetics of lower-crustal eclogitization. *Earth and*  
674 *Planetary Science Letters*, 264(1-2), 226-244.  
675 doi:<https://doi.org/10.1016/j.epsl.2007.09.036>
- 676 Hill, R. (1952). The elastic behaviour of a crystalline aggregate. *Proceedings of the Physical*  
677 *Society. Section A*, 65(5), 349-354.
- 678 Hudson, J. A. (1981). Wave speeds and attenuation of elastic waves in material containing  
679 cracks. *Geophysical Journal International*, 64(1), 133-150.  
680 doi:<https://doi.org/10.1111/j.1365-246X.1981.tb02662.x>
- 681 Jackson, J. A., Austrheim, H., McKenzie, D., & Priestley, K. (2004). Metastability, mechanical  
682 strength, and the support of mountain belts. *Geology*, 32(7), 625-628.  
683 doi:<https://doi.org/10.1130/g20397.1>
- 684 Jakob, J., Andersen, T. B., & Kjöll, H. J. (2019). A review and reinterpretation of the  
685 architecture of the South and South-Central Scandinavian Caledonides—A magma-poor  
686 to magma-rich transition and the significance of the reactivation of rift inherited  
687 structures. *Earth-Science Reviews*, 192, 513-528.  
688 doi:<https://doi.org/10.1016/j.earscirev.2019.01.004>
- 689 Jamtveit, B., Austrheim, H., & Malthe-Sorensen, A. (2000). Accelerated hydration of the  
690 Earth's deep crust induced by stress perturbations. *Nature*, 408(6808), 75-78.  
691 doi:<https://doi.org/10.1038/35040537>

- 692 Jamtveit, B., Bucher-Nurminen, K., & Austrheim, H. (1990). Fluid controlled eclogitization of  
693 granulites in deep crustal shear zones, Bergen arcs, Western Norway. *Contributions to*  
694 *Mineralogy and Petrology*, 104(2), 184-193. doi:<https://doi.org/10.1007/bf00306442>
- 695 John, T., & Schenk, V. (2003). Partial eclogitisation of gabbroic rocks in a late Precambrian  
696 subduction zone (Zambia): prograde metamorphism triggered by fluid infiltration.  
697 *Contributions to Mineralogy and Petrology*, 146(2), 174-191.  
698 doi:<https://doi.org/10.1007/s00410-003-0492-8>
- 699 Jolivet, L., Raimbourg, H., Labrousse, L., Avigad, D., Leroy, Y., Austrheim, H., & Andersen, T.  
700 B. (2005). Softening triggered by eclogitization, the first step toward exhumation during  
701 continental subduction. *Earth and Planetary Science Letters*, 237(3-4), 532-547.  
702 doi:<https://doi.org/10.1016/j.epsl.2005.06.047>
- 703 Kern, H., Gao, S., & Liu, Q.-S. (1996). Seismic properties and densities of middle and lower  
704 crustal rocks exposed along the North China Geoscience Transect. *Earth and Planetary*  
705 *Science Letters*, 139(3), 439-455. doi:[https://doi.org/10.1016/0012-821X\(95\)00240-D](https://doi.org/10.1016/0012-821X(95)00240-D)
- 706 Kim, D., Keranen, K. M., Abers, G. A., & Brown, L. D. (2019). Enhanced Resolution of the  
707 Subducting Plate Interface in Central Alaska From Autocorrelation of Local Earthquake  
708 Coda. *Journal of Geophysical Research: Solid Earth*, 124(2), 1583-1600.  
709 doi:<https://doi.org/10.1029/2018jb016167>
- 710 Kind, R., Yuan, X., & Kumar, P. (2012). Seismic receiver functions and the lithosphere–  
711 asthenosphere boundary. *Tectonophysics*, 536-537, 25-43.  
712 doi:<https://doi.org/10.1016/j.tecto.2012.03.005>
- 713 Klemm, R., John, T., Scherer, E. E., Rondenay, S., & Gao, J. (2011). Changes in dip of subducted  
714 slabs at depth: Petrological and geochronological evidence from HP–UHP rocks  
715 (Tianshan, NW-China). *Earth and Planetary Science Letters*, 310(1-2), 9-20.  
716 doi:<https://doi.org/10.1016/j.epsl.2011.07.022>
- 717 Labrousse, L., Hetényi, G., Raimbourg, H., Jolivet, L., & Andersen, T. B. (2010). Initiation of  
718 crustal-scale thrusts triggered by metamorphic reactions at depth: Insights from a  
719 comparison between the Himalayas and Scandinavian Caledonides. *Tectonics*, 29(5),  
720 TC5002. doi:<https://doi.org/10.1029/2009TC002602>
- 721 Llana-Funez, S., & Brown, D. (2012). Contribution of crystallographic preferred orientation to  
722 seismic anisotropy across a surface analog of the continental Moho at Cabo Ortegal,  
723 Spain. *Geological Society of America Bulletin*, 124(9-10), 1495-1513.  
724 doi:<https://doi.org/10.1130/b30568.1>
- 725 Mavko, G., Mukerji, T., & Dvorkin, J. (2009). *The rock physics handbook: Tools for seismic*  
726 *analysis of porous media*: Cambridge university press.
- 727 Nabelek, J., Hetenyi, G., Vergne, J., Sapkota, S., Kafle, B., Jiang, M., . . . Hi, C. T. (2009).  
728 Underplating in the Himalaya-Tibet collision zone revealed by the Hi-CLIMB  
729 experiment. *Science*, 325(5946), 1371-1374. doi:<https://doi.org/10.1126/science.1167719>
- 730 Pearce, F. D., Rondenay, S., Sachpazi, M., Charalampakis, M., & Royden, L. H. (2012). Seismic  
731 investigation of the transition from continental to oceanic subduction along the western  
732 Hellenic Subduction Zone. *Journal of Geophysical Research: Solid Earth*, 117, B07306.  
733 doi:<https://doi.org/10.1029/2011JB009023>
- 734 Raimbourg, H., Jolivet, L., Labrousse, L., Leroy, Y., & Avigad, D. (2005). Kinematics of  
735 syneclogite deformation in the Bergen Arcs, Norway: implications for exhumation  
736 mechanisms. *Geological Society, London, Special Publications*, 243(1), 175-192.  
737 doi:<https://doi.org/10.1144/gsl.sp.2005.243.01.13>



- 738 Rondenay, S., Abers, G. A., & van Keken, P. E. (2008). Seismic imaging of subduction zone  
739 metamorphism. *Geology*, *36*(4), 275-278. doi:<https://doi.org/10.1130/G24112A.1>
- 740 Saenger, E. H., Krüger, O. S., & Shapiro, S. A. (2004). Effective elastic properties of randomly  
741 fractured soils: 3D numerical experiments. *Geophysical Prospecting*, *52*(3), 183-195.  
742 doi:<https://doi.org/10.1111/j.1365-2478.2004.00407.x>
- 743 Schneider, F. M., Yuan, X., Schurr, B., Mechie, J., Sippl, C., Haberland, C., . . . Negmatullaev,  
744 S. (2013). Seismic imaging of subducting continental lower crust beneath the Pamir.  
745 *Earth and Planetary Science Letters*, *375*, 101-112.  
746 doi:<https://doi.org/10.1016/j.epsl.2013.05.015>
- 747 Schulte-Pelkum, V., Monsalve, G., Sheehan, A., Pandey, M. R., Sapkota, S., Bilham, R., & Wu,  
748 F. (2005). Imaging the Indian subcontinent beneath the Himalaya. *Nature*, *435*(7046),  
749 1222-1225. doi:<https://doi.org/10.1038/nature03678>
- 750 Shewchuk, J. R. (1996). Triangle: Engineering a 2D quality mesh generator and Delaunay  
751 triangulator. In M. C. Lin & D. Manocha (Eds.), *Applied Computational Geometry*  
752 *Towards Geometric Engineering* (Vol. 1148, pp. 203-222). Berlin, Heidelberg: Springer  
753 Berlin Heidelberg.
- 754 Sippl, C., Schurr, B., Tympel, J., Angiboust, S., Mechie, J., Yuan, X., . . . Haberland, C. (2013).  
755 Deep burial of Asian continental crust beneath the Pamir imaged with local earthquake  
756 tomography. *Earth and Planetary Science Letters*, *384*, 165-177.  
757 doi:<https://doi.org/10.1016/j.epsl.2013.10.013>
- 758 Worthington, J. R., Hacker, B. R., & Zandt, G. (2013). Distinguishing eclogite from peridotite:  
759 EBSD-based calculations of seismic velocities. *Geophysical Journal International*,  
760 *193*(1), 489-505. doi:<https://doi.org/10.1093/gji/ggt004>
- 761 Yamato, P., Duretz, T., & Angiboust, S. (2019). Brittle/ductile deformation of eclogites: insights  
762 from numerical models. *Geochemistry, Geophysics, Geosystems*, *20*, 3116–3133.  
763 doi:<https://doi.org/10.1029/2019gc008249>
- 764 Yuan, X., Sobolev, S. V., Kind, R., Oncken, O., Bock, G., Asch, G., . . . Comte, D. (2000).  
765 Subduction and collision processes in the Central Andes constrained by converted  
766 seismic phases. *Nature*, *408*, 958–961. doi:<https://doi.org/10.1038/35050073>
- 767 Zertani, S., John, T., Tilmann, F., Motra, H. B., Keppler, R., Andersen, T. B., & Labrousse, L.  
768 (2019a). Modification of the seismic properties of subducting continental crust by  
769 eclogitization and deformation processes. *Journal of Geophysical Research: Solid Earth*,  
770 *124*, 9731-9754. doi:<https://doi.org/10.1029/2019jb017741>
- 771 Zertani, S., Labrousse, L., John, T., Andersen, T. B., & Tilmann, F. (2019b). The Interplay of  
772 Eclogitization and Deformation During Deep Burial of the Lower Continental Crust—A  
773 Case Study From the Bergen Arcs (Western Norway). *Tectonics*, *38*(3), 898-915.  
774 doi:<https://doi.org/10.1029/2018tc005297>
- 775 Zhong, X., Andersen, N. H., Dabrowski, M., & Jamtveit, B. (2019). Zircon and quartz inclusions  
776 in garnet used for complementary Raman thermobarometry: application to the Holsnøy  
777 eclogite, Bergen Arcs, Western Norway. *Contributions to Mineralogy and Petrology*,  
778 *174*(6), 50. doi:<https://doi.org/10.1007/s00410-019-1584-4>